RKKY interaction in graphene from the lattice Green's function

M. Sherafati and S. Satpathy
Department of Physics, University of Missouri, Columbia, Missouri 65211, USA
(Received 27 August 2010; published 18 April 2011)

We study the exchange interaction J between two magnetic impurities in undoped graphene (the Ruderman-Kittel-Kasuya-Yosida [RKKY] interaction) by directly computing the lattice Green's function for the tight-binding band structure for the honeycomb lattice. The method allows us to compute J numerically for much larger distances than can be handled by finite-lattice calculations as well as for small distances. In addition, we rederive the analytical long-distance behavior of J for linearly dispersive bands and find corrections to the oscillatory factor that were previously missed in the literature. The main features of the RKKY interaction in half-filled graphene are that unlike the $J \propto (2k_F R)^{-2}\sin(2k_F R)$ behavior of an ordinary two-dimensional metal in the long-distance limit, J in graphene falls off as $1/R^3$, shows the $1+\cos[(K-K')\cdot R]$-type oscillations with additional phase factors depending on the direction, and exhibits a ferromagnetic interaction for moments on the same sublattice and an antiferromagnetic interaction for moments on the opposite sublattices as required by particle-hole symmetry. The computed J with the full band structure agrees with our analytical results in the long-distance limit, including the oscillatory factors with the additional phases.

DOI: 10.1103/PhysRevB.83.165425 PACS number(s): 75.30.Hx, 75.10.Lp, 75.20.Hr

I. INTRODUCTION

Graphene has attracted considerable attention recently due to its linear energy dispersion, where the excitations are massless Dirac fermions, which could lead to physical behavior different from that of the standard two-dimensional systems. The Ruderman-Kittel-Kasuya-Yosida (RKKY) interaction is the exchange interaction between two magnetic impurities mediated by the conduction electrons of the host and is a fundamental quantity of interest.[1,2] Earlier works on the RKKY interaction in graphene[3–6] have mostly used a continuum model with a linearly dispersive band structure with two Dirac cones at the corners of the Brillouin zone (BZ) or have used exact diagonalization on a finite-size lattice.[7] As pointed out by Saremi,[3,8] for a bipartite lattice with nearest-neighbor (NN) interactions, particle-hole symmetry leads to a ferromagnetic interaction on the same sublattice and an antiferromagnetic interaction for the opposite sublattices.

The continuum-limit, linearly dispersive Dirac cone approximation is expected to be good in the long-distance limit $R \to \infty$ and allows an analytical solution. However, it requires the use of a cutoff function, without which the contributions from the higher energy states add up to produce a diverging and oscillatory result. If a sharp energy cutoff is used, it produces a J that oscillates with distance violating the particle-hole symmetry. To address this problem, a cutoff function approach[3] has been used, where the higher-momentum contributions are damped out slowly, with the length scale of damping taken to infinity as the limiting case. While this approach yields a reasonable result, it is not *a priori* obvious if some systematic error is not introduced by such a procedure. In fact, using exact diagonalization on finite lattices, Black-Schaffer[7] extracted J values that differed from Saremi's results both in the prefactors and, for J_{AB}, in the oscillatory factor as well. On the other hand, the finite-lattice calculations in turn suffer from the deficiency that the distance between the impurities can not be too large, and extra interactions between the moments get introduced due to the supercell geometry.

In order to address these issues, we use a direct computation of the lattice Green's function at zero temperature ($T = 0$) to compute the RKKY interaction with the full tight-binding band structure. The method allows us to numerically calculate the RKKY interaction for very large distances, which is impractical to obtain from the finite-lattice calculations. In addition, we obtain analytical results for the long-distance behavior of J by using an approach slightly different from that of Saremi,[3] which allows us to obtain the proper phase factors in the RKKY oscillations that were missed in previous works. We note that for obtaining the proper oscillatory factors of J, it is important to include carefully the phase factors of the electronic wavefunctions around the Dirac points.

II. FORMULATION

We consider the tight-binding Hamiltonian for graphene including a contact interaction with the magnetic centers, namely,

$$\mathcal{H} = \sum_{\langle ij\rangle\sigma} t_{ij} c^\dagger_{i\sigma} c_{j\sigma} + \text{H.c.} - \lambda \sum_p \vec{S}_p \cdot \vec{s}_p, \tag{1}$$

where i is the combined site-sublattice index, $\langle ij\rangle$ denotes summation over distinct pairs of NN sites, σ denotes the electron spin, the p summation runs over the magnetic centers, and $\vec{s}_p = (\hbar/2)\sum_{\mu\nu} c^\dagger_{p\mu}\vec{\tau}_{\mu\nu}c_{p\nu}$ is the itinerant electron spin density. The results can be easily generalized if the hopping integrals t_{ij} are retained beyond the NN. However, direct numerical computations showed that neglecting the higher neighbor terms does not change J significantly, since the magnitudes of the hopping beyond the NNs are relatively small in graphene.[9] The NN hopping parameter in graphene is $t = -2.56$ eV as obtained by fitting the tight-binding bands to the density-functional band calculations.[9]

A. Hamiltonian preliminaries

We define the basis of the sublattice Bloch functions

$$c^\dagger_{k\alpha} = N^{-1/2}\sum_i e^{ik\cdot r_{i\alpha}} c^\dagger_{i\alpha}, \tag{2}$$

where $\alpha = A$ or B are the two sublattices, with $r_{i\alpha} = R_i + \tau_\alpha$ being the lattice position of α-th atom in the i-th unit cell (usually $\tau_A = 0$ and τ_B is a NN distance vector). In this basis, the unperturbed Hamiltonian is given by

$$\mathcal{H}_k = \begin{pmatrix} 0 & f(k) \\ f^*(k) & 0 \end{pmatrix}, \tag{3}$$

where $f(k) = t\ (e^{ik\cdot d_1} + e^{ik\cdot d_2} + e^{ik\cdot d_3})$ and d_1, d_2, and d_3 are the NN position vectors. The Hamiltonian expression near a Dirac point K_D takes the form $f(q + K_D) = v_F q\ \phi(q)$, with different phases $\phi(q)$ at different Dirac points as indicated in Fig. 1, where q is the momentum measured from the neighboring Dirac point, $q = k - K_D$. Diagonalization of the Hamiltonian yields the familiar linear dispersion near the Dirac points, namely, $E_{q,\pm} = \pm|v_F|q$ with the Fermi velocity $v_F \equiv 3ta/2$, which is defined to be negative throughout this paper, t being negative, and a is the bond length. The $\pm$ signs denote the conduction and valence bands, respectively. The corresponding eigenstates are

$$|\Psi_k^\pm\rangle = 2^{-1/2}(\pm f(k)/|f(k)|c_{kA}^\dagger + c_{kB}^\dagger)|0\rangle. \tag{4}$$

For physical interpretation, it is convenient to write down the real-space wavefunctions in the central cell by using Eq. (2). Defining the central cell to be made out of atom A at the origin and atom B at the position $\tau_B = \vec{d}_3$ (Fig. 2), we have the two-component central-cell wavefunctions

$$\Psi_{K'}^\pm = \frac{1}{\sqrt{2}}\begin{pmatrix} \mp e^{-i\theta_q} \\ 1 \end{pmatrix} \text{ and } \Psi_K^\pm = \frac{1}{\sqrt{2}}\begin{pmatrix} \pm e^{i\theta_q} \\ 1 \end{pmatrix}, \tag{5}$$

which have been written for momenta near the two Dirac points. This is obtained by expanding the coefficient $f(k)/|f(k)|$ of the A-sublattice Bloch function in Eq. (4) and multiplying the B-sublattice Bloch function coefficient, which is 1, by the phase factor $e^{ik\cdot d_3}$ following Eq. (2). The wave functions [Eq. (5)] can also be obtained by numerical diagonalization of Hamiltonian [Eq. (3)]. The wavefunction for any other atom located in the unit cell defined by R_i is obtained by multiplying the central-cell wavefunction with the Bloch factor $e^{ik\cdot R_i}$. A different definition of the central cell will obviously change Eq. (5); e.g., the cell defined by $\tau_A = 0$ and $\tau_B = d_1$ will lead to an extra phase factor $e^{\mp 2\pi i/3}$ in the second component in Eq. (5). Similarly, if the sublattice Bloch functions [Eq. (2)] are defined with a $-k$ in the exponent on the right-hand side, the wavefunctions around K and K' in Eq. (5) become interchanged. Equation (5) leads to the usual interpretation of the wavefunctions as pseudospins, with the corresponding Hamiltonians $\mathcal{H}_{K'} = -|v_F|\vec{\sigma}\cdot\vec{q}$ and $\mathcal{H}_K = |v_F|\vec{\sigma}^*\cdot\vec{q}$ near the Dirac points with the Pauli matrices $\vec{\sigma} = (\sigma_x, \sigma_y)$ and $\vec{\sigma}^* = (\sigma_x, -\sigma_y)$.

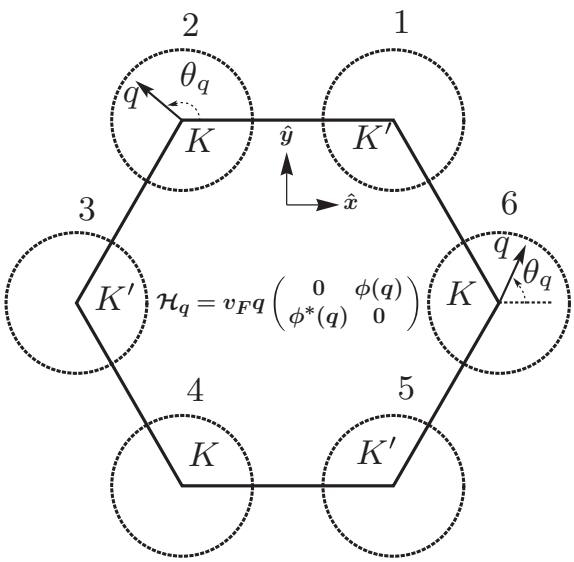

FIG. 1. The Hamiltonian near the Dirac points in the first BZ with $\phi(q) = -e^{i(\pi/3-\theta_q)}$, $e^{i(\pi/3+\theta_q)}$, $e^{-i\theta_q}$, $-e^{i(2\pi/3+\theta_q)}$, $e^{i(2\pi/3-\theta_q)}$, $-e^{i\theta_q}$, for the first through sixth Dirac points (K_1 to K_6) as labeled. The small momentum q is the deviation from the corresponding Dirac point ($k = K_D + q$), and $\theta_q = \tan^{-1}(q_y/q_x)$ is the polar angle of q with respect to $K_1 - K_2$, chosen as the $\hat{x}$ direction as shown. These phase factors are important as they determine the oscillatory behavior of J_{AB}. Note that the $\hat{x}$ direction could be defined by any adjacent pair of Dirac points K'–K. These phase factors depend on the choice of the sublattice Bloch functions as discussed in the text; those presented in the figure and used throughout this paper correspond to the choice of the sublattice Bloch functions given by Eq. (2).

An alternative expression for the sublattice Bloch functions is sometimes used in the literature, where they are defined without the phase factor $e^{ik\cdot\tau_\alpha}$ on the individual sites,[10] so that instead of Eq. (2), we have $c_{k\alpha}^{\prime\dagger} = N^{-1/2}\sum_i e^{ik\cdot R_i}c_{i\alpha}^\dagger$. The matrix elements in the Hamiltonian (3) then change to $f'(k) = f(k)e^{-ik\cdot d_3} = t\ (e^{ik\cdot T_1} + e^{ik\cdot T_2} + 1)$. The low-energy expression near Dirac points is given by $f'(q + K_D) = v_F q\ \phi'(q)$, where $\phi'(q) = e^{-i\theta_q}$ near K' and $-e^{i\theta_q}$ near K. The benefit of this choice is that contrary to $\phi(q)$, the phase $\phi'(q)$ is the same for all Dirac points K or K', irrespective of their locations in the hexagonal BZ. However, with this choice, care must be taken to use the cell positions R_i rather than the actual atom positions $r_{i\alpha}$ in obtaining the wavefunction on a particular atom from the central-cell wavefunction, an error not uncommon to find in the literature. The wavefunctions [Eq. (5)] as well as its interpretation in terms of the pseudospins remain unchanged, irrespective of the choice of the sublattice Bloch functions.

The exchange integral J, or any other physical quantity for that matter, is independent of the choice of the basis functions, but care must be taken to incorporate the appropriate phase factors in the calculations. We work with the first choice of the sublattice Bloch functions [Eq. (2)] throughout this paper.

B. Expression for the exchange interaction

In the linear response theory, the exchange interaction may be obtained by first computing the perturbed wavefunctions due to the magnetic impurity located at the origin from the Lippmann-Schwinger equation $|\Psi\rangle = |\Psi^0\rangle + G^0V|\Psi\rangle$, from which the energy due to the second magnetic impurity located at R is computed from the first-order perturbation theory, so that $E(R) = \langle\Psi|V(R)|\Psi\rangle$. Note that R is the actual position of the atom, in contact with the impurity, and not just the position of the unit cell, in which it is located. For a contact interaction

between the magnetic impurity and the conduction electrons, $V = -\lambda\ \vec{S}\cdot\vec{s}\ \delta(\vec{r})$, $E(R)$ may be written in the Heisenberg form

$$E(R) = J\vec{S}_1\cdot\vec{S}_2, \tag{6}$$

where the exchange integral $J = (\lambda^2\hbar^2/4)\ \chi(0,R)$ and χ is the spin-independent susceptibility.

For a spin-independent perturbation, the standard susceptibility $\chi(r,r') = \delta n(r)/\delta V(r')$ is written in terms of the unperturbed retarded Green's functions

$$\chi(r,r') = -\frac{2}{\pi}\int_{-\infty}^{E_F} dE\ \mathrm{Im}[G^0(r,r',E)G^0(r',r,E)], \tag{7}$$

where the integration is over the occupied states. Here G^0 is the Green's function for a single spin channel and is spin-independent, while in the definition of the susceptibility, $\delta V(r')$ is a spin-independent perturbation, and $\delta n(r)$ is the change in the total charge density *including* both spins.

This result can be easily extended to the case of graphene to yield

$$\chi_{\alpha\beta}(r,r') = -\frac{2}{\pi}\int_{-\infty}^{E_F} dE\ \mathrm{Im}\big[G^0_{\alpha\beta}(r,r',E)G^0_{\beta\alpha}(r',r,E)\big], \tag{8}$$

where α,β are the sublattice indices, A or B, r,r' denote the lattice positions of the two magnetic centers located on the sublattice α and β, respectively, and the sublattice susceptibility is as usual $\chi_{\alpha\beta}(r,r') \equiv \delta n_\alpha(r)/\delta V_\beta(r')$. The expression for the susceptibility is obtained by noting that the charge density is given by $n_\alpha(r) = -\frac{2}{\pi}\int_{-\infty}^{E_F} dE\ \mathrm{Im}\ G_{\alpha\alpha}(r,r,E)$ and obtaining the charge difference $\delta n_\alpha(r)$ induced by the perturbation $\delta V_\beta(r')$ from the Dyson equation $G = G^0 + G^0VG$.

Now, for a spin-dependent perturbation, the exchange interaction $J_{\alpha\beta}(R)$ between impurities located at the sites $(\alpha,0)$ and (β,R) may be written in terms of the above spin-independent susceptibility

$$J_{\alpha\beta}(R) = \frac{\lambda^2\hbar^2}{4}\chi_{\alpha\beta}(0,R). \tag{9}$$

The calculation of the exchange interaction thus boils down to the computation of the lattice Green's functions and a quadrature over the energy following Eq. (8).

III. CALCULATION OF THE GREEN'S FUNCTIONS

We compute the real-space Green's function by two different approaches, namely, the direct integration method and the recursive technique of Horiguchi.[11] In the first method, the real-space Green's functions are calculated by numerically integrating the momentum-space Green's functions

$$G^0_{\alpha\beta}(r,r',E) = \frac{1}{\Omega_{\mathrm{BZ}}}\int d^2k e^{ik\cdot(r-r')}G^0_{\alpha\beta}(k,E). \tag{10}$$

Here $G^0 = (E + i\eta - \mathcal{H}_0)^{-1}$ and the matrix elements are taken in the same basis of the sublattice Bloch functions $|k\alpha\rangle$ corresponding to the operator $c^\dagger_{k\alpha}$ defined in Eq. (2); the subscripts of $r_{i\alpha}$ have been dropped for simplicity of notation. So the positions r and r' refer to the actual positions of the atoms and not just to the positions of the cells that they belong to. The matrix elements are then

$$G^0_{\alpha\beta}(k,E) = \langle k\alpha|G^0(E)|k\beta\rangle = \begin{pmatrix} G^0_{AA} & G^0_{AB} \\ G^0_{BA} & G^0_{BB}\end{pmatrix}$$
$$= (E + i\eta - \mathcal{H}_k)^{-1} = \frac{E + i\eta + \mathcal{H}_k}{(E+i\eta)^2 - f^*(k)f(k)}. \tag{11}$$

The BZ integral in Eq. (10) was evaluated by taking up to $N_k = 10^6$ k-points in the full BZ, and a small value for the infinitesimal parameter $\eta = 0.005$ is used. To ensure convergence, we must have $\Delta k \ll 1/R$, where Δk is the size of the interval in the grid of k mesh points. This method is straightforward and computationally robust but slow, while the Horiguchi recursive technique, discussed below, is fast, but it has stability problems[12] for larger distances. We found that the Horiguchi method becomes unstable for distances $|r - r'| = R \gtrsim 7a$. While both methods gave nearly identical results for the distances where the Horiguchi method is stable, because of this stability problem, all computed values of J were obtained from the Green's functions calculated from the direct integration method following Eq. (10).

It is worth noting the symmetry properties of the Green's functions, which immediately follow from the above equations and the expression for $\mathcal{H}_k$, namely, that $G^0_{AA}(R,0,E) = G^0_{BB}(R,0,E)$ and $G^0_{AB}(0,R,E) = G^0_{BA}(R,0,E)$, leading to the results, which is also obvious on physical grounds:

$$J_{AA}(R) = J_{BB}(R) \text{ and } J_{AB}(R) = J_{BA}(-R). \tag{12}$$

In the second method, the Horiguchi recursive technique,[11] the Green's functions for the honeycomb lattice are expressed in terms of those for the triangular lattice, which in turn are

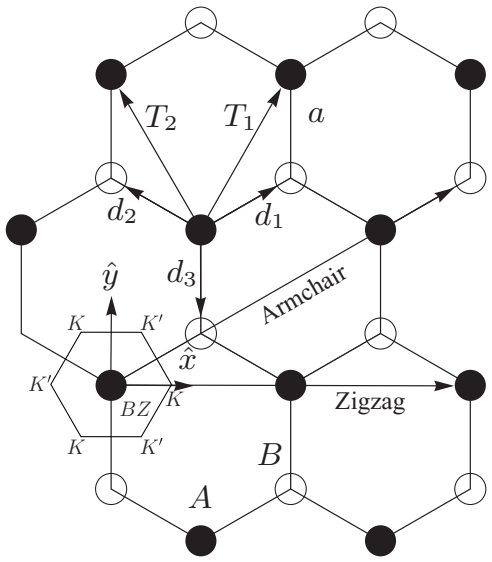

FIG. 2. The graphene honeycomb lattice with two different sublattices, shown as full and open circles. The figure also shows the orientation of the BZ and two common directions in the direct lattice (zigzag and armchair). T_1 and T_2 are the two primitive translation vectors of the direct lattice, and the three NN distance vectors are indicated by d_1, d_2, and d_3.

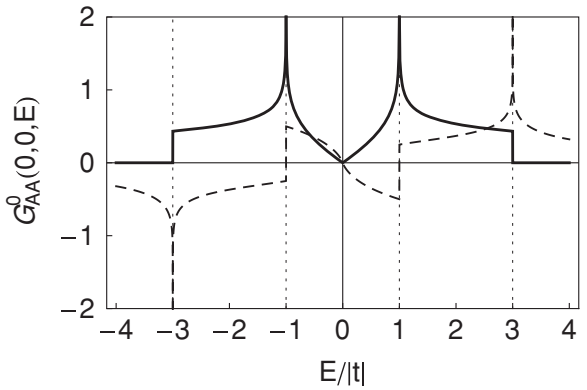

FIG. 3. On-site Green's function Re $G^0_{AA}(0,0,E)$ (dashed line) and $-\mathrm{Im}\, G^0_{AA}(0,0,E)$ (full line) computed from Eq. (13).

expressed in terms of the elliptic integrals. For example, the expression for the on-site Green's function is given by

$$G^0_{AA}(0,0,z) = \frac{z}{4\pi} g(z') \tilde{K}[k(z')], \tag{13}$$

where $z = E + i\eta$, $z' = (z^2 - 3)/2$, $g(z') = 8[(2z'+3)^{1/2} - 1]^{-3/2}[(2z'+3)^{1/2}+3]^{-1/2}$, $k(z') = 2^{-1} g(z')(2z'+3)^{1/4}$,

$$\tilde{K}(k(z')) = \begin{cases} K(k(z')) & \text{for } \mathrm{Im}\, k \cdot \mathrm{Im}\, z' < 0 \\ K(k(z')) + 2i\, K(\sqrt{1-k^2(z')}) & \text{for } \mathrm{Im}\, k > 0 \text{ and } \mathrm{Im}\, z' > 0 \\ K(k(z')) - 2i\, K(\sqrt{1-k^2(z')}) & \text{for } \mathrm{Im}\, k < 0 \text{ and } \mathrm{Im}\, z' < 0 \end{cases}$$

and $K(k)$ is the elliptic integral

$$K(k) = \int_0^{\pi/2} \frac{1}{(1 - k^2 \sin^2\theta)^{1/2}}\, d\theta. \tag{14}$$

The elliptic integral with complex modulus was evaluated following established procedures and the Arithmetic-Geometric Mean Method,[13,14] and $\eta = 10^{-6}$ was used.

The computed result for the on-site Green's function obtained from Eq. (13) is shown in Fig. 3, and one sees the familiar density of states, which is proportional to the imaginary part: $\rho_0(E) = -\pi^{-1}\mathrm{Im}\, G^0_{AA}(0,0,E)$, where $\rho_0(E)$ is the density of states per atom per spin. For low energy $E \to 0$, Eq. (13) yields the well-known linear density of states

$$\rho_0(E) = \frac{A_c}{2\pi} \frac{|E|}{v_F^2}, \tag{15}$$

where A_c is the area of the unit cell. Similarly, one can compute the Green's functions for a few lattice vectors R [specifically, $R \equiv (l,m) = (0,0),(2,0)$,and $(4,0)$, for the triangular lattice using Horiguchi's notation], from which the remaining Green's functions for both the triangular as well as the honeycomb lattice can be computed using the recursion relations.

In Fig. 4, we have plotted the Green's function $G^0_{AA}(R,0,E)$ with a specific $R = 7\sqrt{3}a(1,0)$ along the zigzag direction and also the product of the real and the imaginary parts, which enters as the integrand in the calculation of J [Eq. (8)] , to be integrated over the occupied states between $E = -\infty$ and zero ($E_F = 0$ for the undoped graphene). As seen in the figure, the integrand is a rapidly oscillating function, with a small net result for J.

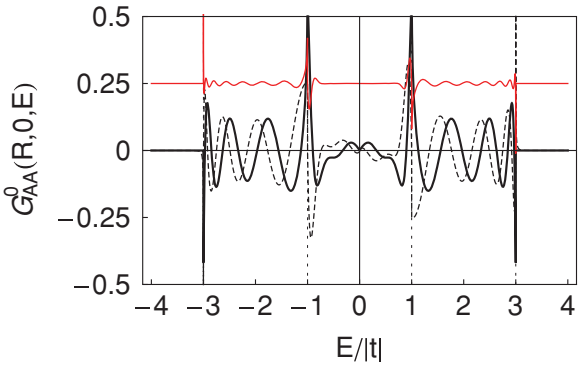

FIG. 4. (Color online) Real (dashed line) and imaginary (full line) parts of the Green's function $G^0_{AA}(R,0,E)$ with $R = 7\sqrt{3}a(1,0)$ obtained from the Horiguchi recursive method. Red (thin) line shows the product of the real and imaginary parts, which is displaced by +0.25 along the y axis.

IV. EXCHANGE INTERACTION

Before we present the results of the full calculations, we derive the long-distance behavior of J with the linearly-dispersive band structure. This is reasonable as the long-distance behavior is necessarily determined by the small momentum states, for which the linear-band approximation is excellent. As has been pointed out in the literature,[3,7] the RKKY interaction shows oscillations as a function of distance because of the interference between spin densities originating from the two Dirac points in the BZ. However, there is no consensus regarding the form of the oscillation, and we find important differences from the earlier results.

A. Magnetic impurities on the same sublattice

To derive the long-distance oscillatory behavior of the RKKY interaction, we first obtain the Green's functions for small energies (which necessarily determine the long-distance behavior) and use these to evaluate the integral in the expression [Eq. (8)] for the susceptibility. For small energies, the contribution to the integral in Eq. (10) comes from the two Dirac points in the BZ, so that the equation becomes

$$G^0_{\alpha\beta}(R,0,E) = \frac{1}{\Omega_{\mathrm{BZ}}} \int d^2q\, e^{iq\cdot R}\left[e^{iK\cdot R} G^0_{\alpha\beta}(q+K,E) + e^{iK'\cdot R} G^0_{\alpha\beta}(q+K',E)\right], \tag{16}$$

where K and K' are the two Dirac points and R is the distance between the two magnetic centers.

For $\alpha = \beta$, i.e., if the two sublattices are the same, these two Green's functions in the kernel become the same, namely, $G^0_{AA}(q,E) = (E+i\eta)[(E+i\eta)^2 - v_F^2 q^2]^{-1}$ as seen from Eq. (11). The exponential factor may be expanded (Jacobi-Anger expansion[15]) in terms of the Bessel functions as

$$e^{iq\cdot R} = J_0(qR) + 2\sum_{n=1}^{\infty} i^n J_n(qR)\cos[n(\theta_q - \theta_R)], \tag{17}$$

where θ_q and $\theta_R = \tan^{-1}(y/x)$ are the polar angles of the vectors $\vec{q}$ and $\vec{R}$ with respect to the chosen x axis, respectively, as explained in Fig. 1; for example, along the armchair

direction, shown in Fig. 2, we have $\theta_R = \frac{\pi}{6}$ for the distance R of atoms A or B from the origin.

Then integration over θ_q yields

$$G^0_{AA}(R,0,E) = (e^{iK\cdot R} + e^{iK'\cdot R})g_{AA}(R,E), \tag{18}$$

where

$$g_{AA}(R,E) = \frac{2\pi}{\Omega_{\rm BZ}}\int_0^{q_c} q dq\, J_0(qR)G^0_{AA}(q,E), \tag{19}$$

and a momentum cutoff q_c has been introduced. Because the phase factor sum in Eq. (18) turns out to be real, we get a similar expression for $G^0_{AA}(0,R,E)$, and plugging these in Eq. (8), we immediately get

$$\chi_{AA}(0,R) = I_{AA}(R)\times\{1+\cos[(K-K')\cdot R]\} \tag{20}$$

with the prefactor

$$I_{AA}(R) = -\frac{4}{\pi}\int_{-\infty}^{E_F} dE\ {\rm Im}\,[g_{AA}(R,E)]^2. \tag{21}$$

The large distance behavior of J is controlled by small momentum states, and one may try to evaluate this by taking the cutoff $q_c\to\infty$ for the ease of performing the integrals. In this case the integral in Eq. (19) can be expressed in terms of the modified Bessel function of the second kind, namely, $g_{AA} = -2\pi\Omega_{\rm BZ}^{-1}(E/v_F^2)K_0(iER/v_F)$.[16,17] This in turn may be expressed in terms of Bessel and Neumann functions[18] with real arguments to yield the kernel ${\rm Im}\,[g_{AA}(R,E)]^2 = (2\pi^4)\Omega_{\rm BZ}^{-2}v_F^{-2}R^{-2}y^2J_0(y)Y_0(y)$, where $y = ERv_F^{-1}$. Thus Eq. (21) becomes

$$I_{AA}(R) = \frac{8\pi^3}{\Omega_{\rm BZ}^2 v_F}R^{-3}\int_0^\infty dy y^2 J_0(y)Y_0(y). \tag{22}$$

The R^{-3} dependence clearly emerges; however, the integral does not converge. Following Saremi,[3] we multiply the integrand by a cutoff function $f(y,y_0)$, perform the integral, and take the limit $y_0\to\infty$. In this limit, the cutoff function $f(y,y_0)\to 1$, so that the integral in Eq. (22) is recovered. We have tried three different cutoff functions, namely, $f(y,y_0) = \exp(-y/y_0)$, $\exp(-y^2/y_0^2)$, or $y_0^2(y_0^2+y^2)^{-1}$, and in each case we find the same limit: $\lim_{y_0\to\infty}\int_0^\infty dy y^2 J_0(y)Y_0(y)f(y,y_0) = 1/16$. Thus we immediately get $I_{AA}(R) = 9(64\pi t)^{-1}a^3/R^3$, which leads to the exchange interaction for the same sublattice

$$J_{AA}(R) = -C\times\frac{1+\cos[(K-K')\cdot R]}{(R/a)^3}, \tag{23}$$

where $C\equiv -9\lambda^2\hbar^2/(256\pi t)$ is a positive quantity, since $t<0$ in graphene. We note that the oscillatory factor is identical to the expression derived by Saremi;[3] however, we have an additional scaling factor of $3/2$ for the magnitude of J_{AA}. From finite-size calculations, Black-Schaffer[7] extracted a scaling factor different from ours or that of Saremi; however, we note that such factors are difficult to extract from numerical results, especially from finite-size calculations.

The expression for J_{AA}, Eq. (23), is valid for all directions including the zigzag and the armchair directions, and K and K' are any two adjacent Dirac points in the BZ. It is easy to see that while the oscillatory factor $1+\cos[(K-K')\cdot R]$ repeats in triplets as $2, 1/2, 1/2, \ldots$ with distance R along the zigzag direction, it is always two for the armchair direction. Because of this, the magnitude of J_{AA} oscillates for the zigzag direction but not for the armchair direction, always, however, remaining ferromagnetic as required by the particle-hole symmetry.

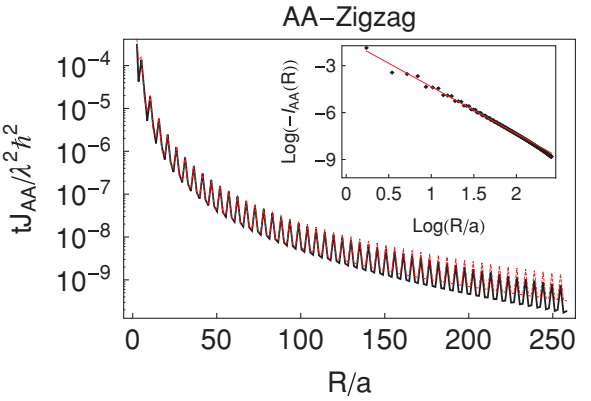

FIG. 5. (Color online) Exchange interaction J_{AA} between two impurities on the same sublattice. Black solid lines are the results with the full tight-binding band structure, and the red dashed lines indicate the long-distance behavior as obtained from Eq. (23) using linear dispersion. The inset shows the log plot showing the long-distance R^{-3} behavior, while there are noticeable differences for small R, especially visible in the inset. Note that since t is negative for graphene, J_{AA} is also negative, indicating a ferromagnetic interaction.

The calculated results for J_{AA} using the full band structure following the methods of Secs. II and III are shown in Fig. 5 for the zigzag direction and in Fig. 6 for the armchair direction. Both follow the long-distance behavior of Eq. (23) quite well beginning with surprisingly small distances.

B. Magnetic impurities on two different sublattices

We now turn to J_{AB}, where the two impurities are located on different sublattices. The needed Green's functions, in the small q limit, are obtained from Eq. (11) to yield

$$G^0_{BA}(q+K_D,E) = \pm\frac{v_F q\, e^{-i(\pi/3\pm\theta_q)}}{(E+i\eta)^2 - v_F^2q^2}, \tag{24}$$

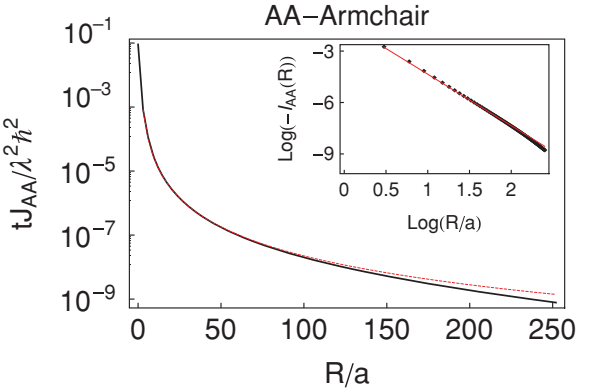

FIG. 6. (Color online) Same as Fig. 5 for the armchair direction. For this direction, consistent with Eq. (23), there are no oscillations in J unlike the zigzag direction (Fig. 5).

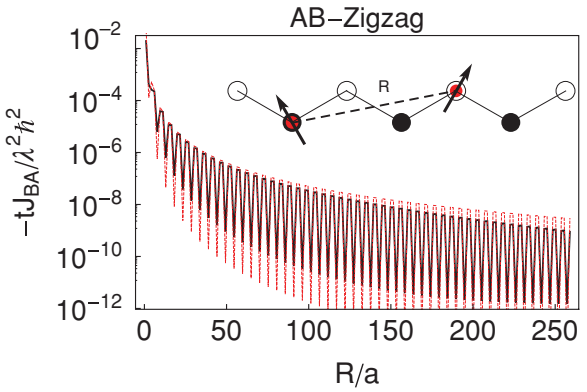

FIG. 7. (Color online) J_{BA} for the zigzag direction. Black solid line is the result of the full calculation, and the red dashed line is obtained from Eq. (30).

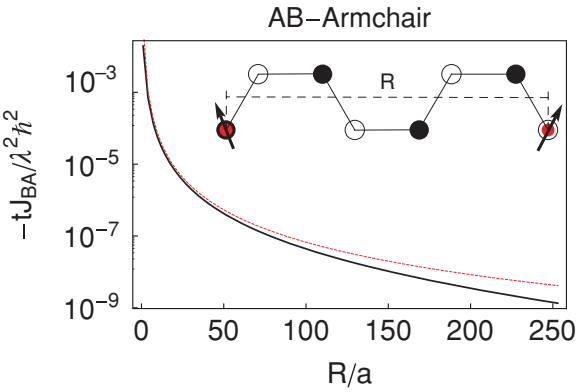

FIG. 8. (Color online) Same as Fig. 7 for the armchair direction.

where $\pm$ signs are for the two Dirac points $K_D = K$ and K', respectively. Here we have chosen a BZ that includes the K_1 and K_2 points, and the corresponding phase factors in the Hamiltonian have been retained (see Fig. 1). The next step is to obtain $G^0_{BA}(R,0,E)$ by the momentum space integration using Eq. (16). The same Jacobi-Anger expansion for $e^{iq\cdot R}$ [Eq. (17)] may be used as before except that now the extra phase factor $e^{\pm i\theta_q}$ appears in the angle integral while performing the integration in Eq. (16). Using the result

$$\int_0^{2\pi} d\theta_q e^{\pm i\theta_q} \cos[n(\theta_q - \theta_R)] = \begin{cases} 0 & \text{if} \quad n \neq 1, \\ \pi e^{\pm i\theta_R} & \text{if} \quad n = 1, \end{cases} \tag{25}$$

we get after some algebra, the result $G^0_{BA}(R,0,E) = \alpha \; g_{BA}(R,E)$, where $\alpha = e^{-i\pi/3}(e^{i(K\cdot R-\theta_R)} - e^{i(K'\cdot R+\theta_R)})$, which turns out to be pure imaginary, and

$$g_{BA}(R,E) = \frac{2\pi i v_F}{\Omega_{\rm BZ}} \int_0^{q_c} dq \frac{q^2 J_1(qR)}{(E+i\eta)^2 - v_F^2 q^2}. \tag{26}$$

Similarly we find $G^0_{AB}(0,R,E) = -\alpha^* \; g_{BA}(R,E)$. Finally, using Eq. (8), the susceptibility becomes

$$\chi_{BA}(R,0) = I_{BA}(R) \times \{1 + \cos[(K-K')\cdot R + \pi - 2\theta_R]\} \tag{27}$$

with the prefactor

$$I_{BA}(R) = \frac{4}{\pi} \int_{-\infty}^{E_F} dE \; \text{Im}\,[g_{BA}(R,E)]^2. \tag{28}$$

We can now proceed to evaluate J_{BA} in the long-distance limit in a fashion similar to the previous subsection. We find that $g_{BA} = 2\pi\Omega_{\rm BZ}^{-1}(E/v_F^2)K_1(iER/v_F)$, where K_1 is the first-order modified Bessel function of the second kind. Expressing this in terms of Bessel and Neumann functions and using a cutoff function as before, we finally get

$$I_{BA}(R) = \frac{8\pi^3}{\Omega_{\rm BZ}^2 v_F} R^{-3} \lim_{y_0\to\infty} \int_0^\infty dy y^2 J_1(y) Y_1(y) f(y,y_0). \tag{29}$$

The result for this integral is $-3/16$, so that collecting all terms, the exchange interaction becomes

$$J_{BA}(R) = 3C \times \frac{1 + \cos[(K-K')\cdot R + \pi - 2\theta_R]}{(R/a)^3}. \tag{30}$$

Note that the equation is valid for any direction of R and for any choice of the two Dirac points K and K' (they have to be adjacent to each other, of course, so that they are within a single unit cell in the reciprocal lattice), so long as we define the angle θ_R to be with respect to the chosen K'–K vector. One can check that these equations yield the same results for J for different equivalent directions R as expected from symmetry. Note that J_{BA} has the extra factor $\pi - 2\theta_R$ in the argument of the cosine as compared to J_{AA}, which comes from the interference of the contributions to the Green's functions [Eq. (16)] from the two Dirac points. For the zigzag direction along K'–K, the oscillatory part of Eq. (30) agrees with the Black-Schaffer result,[7] since the angle θ_R vanishes for large R. However, our result is valid for all directions, and furthermore for the armchair directions, the angle θ_R is never zero (see Fig. 2), so that this phase factor must be retained in Eq. (30).

The oscillatory behaviors seen in the full calculations for J_{BA} presented in Figs. 7 and 8 are contained in Eq. (30). For the zigzag direction, taking $K-K' = 4\pi(3\sqrt{3}a)^{-1}(-1,0)$ and $R = \vec{d}_1 + \sqrt{3}an\hat{x}$, where n is an integer, the oscillatory factor in Eq. (27) becomes $1 + \cos[(4n-1)\pi/3 + 2\theta_R]$. In the limit $R \to \infty$, $\theta_R \to 0$, so that this factor repeats in the sequence of the triplet numbers: 0, 3/2, 3/2 as R is increased. For a finite R, $\theta_R \neq 0$, so that we never get exactly the zero in the triplet, but rather a small number, which is faithfully reproduced in the full calculations shown in Fig. 7, where two values of J are close in magnitude, while the next one is lower by about three orders of magnitude. For the armchair direction, $R = 2^{-1}a(3n+1)(\sqrt{3},1)$, n being an integer and $\theta_R = \pi/6$, so that the oscillatory factor in Eq. (27) is always 2. The exchange interaction thus changes smoothly with distance without any oscillations, as seen from Fig. 8.

C. Interaction between impurities on plaquettes

The plaquette impurities, where the magnetic impurities are located at high-symmetry points rather than at single lattice sites, are of interest because a number of atoms and

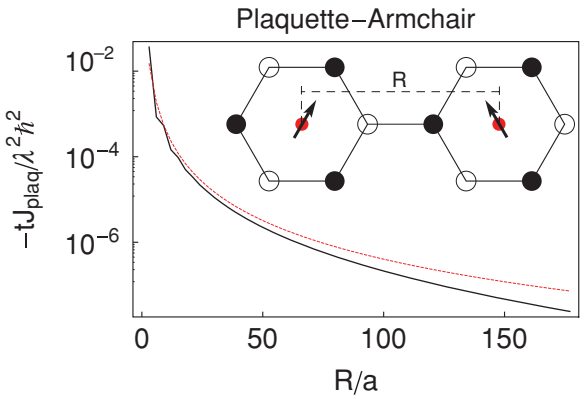

FIG. 9. (Color online) Magnetic interaction J for the hexagonal plaquette along the armchair direction. Black solid line is the result of the full-band calculation, and the red dashed line is obtained from Eq. (32).

small molecules may be favored to occupy such positions. For instance, the impurity may be located midway at a bond center and may interact with the two neighboring sites on the bond. In these situations, the interaction term in Eq. (1) may be replaced by

$$\mathcal{H}_{\rm int} = -\lambda \vec{S}_1 \cdot \sum_p \vec{s}_p - \lambda \vec{S}_2 \cdot \sum_{p'} \vec{s}_{p'}, \tag{31}$$

where the summations are performed over the lattice sites with which the impurity spins $\vec{S}_j$ interact (six sites if the impurity is located at the hexagon center, and two if it is on the bond center). Assuming that the interaction strength is small ($\lambda \ll |t|$), the interaction J for these plaquette impurities may be obtained by simply summing over the individual site-site interactions already obtained in Sec. III, so that $J = \sum_{p,p'} J_{pp'}$.

These results are shown in Figs. 9 and 10 for the hexagonal plaquettes and in Fig. 11 for impurities located on the bond centers. For the hexagonal plaquettes, as has been pointed out earlier,[3,7] the oscillating cosine factors present in the site interactions, J_{AA} and J_{BA}, cancel out both for the armchair and for the zigzag hexagonal plaquette, leading to the single result valid for both cases:

$$J_{\rm plaq}(R) = 36C \times (R/a)^{-3}, \tag{32}$$

which is a net antiferromagnetic interaction.

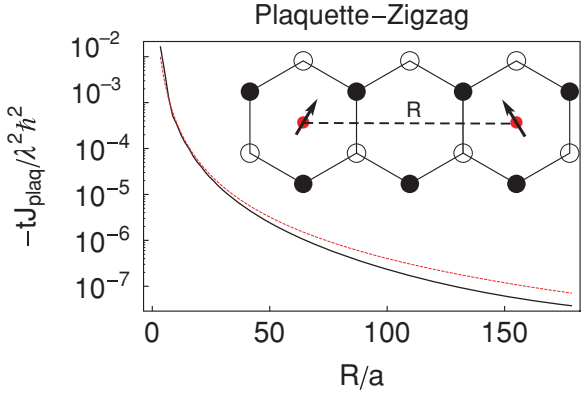

FIG. 10. (Color online) Same as Fig. 9 for the zigzag direction.

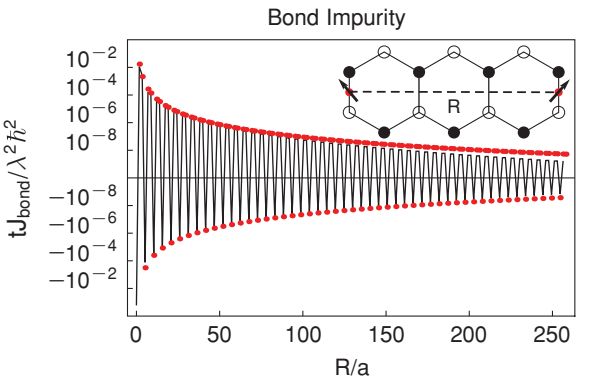

FIG. 11. (Color online) Magnetic interaction $J_{\rm bond}$ between two impurities located on bond centers obtained from the full calculation (solid line) and the linear-band long-distance limit Eq. (33) (red dots).

For impurities located midway between the bond centers along the zigzag direction, we find an oscillating interaction, in the long-distance limit,

$$J_{\rm bond}(R) = 4C \times \frac{1 - 2\cos[(K - K') \cdot R]}{(R/a)^3}. \tag{33}$$

As distance R is increased, the numerator changes with the repeat sequence of -1, 2, and 2, leading to an interaction that is antiferromagnetic every third site and ferromagnetic otherwise. The results from the full calculation is compared to the long-distance limit result, Eq. (33), in Fig. 11.

V. SUMMARY AND DISCUSSION

In summary, we studied the RKKY interaction between the magnetic impurities in the honeycomb lattice by evaluating the Green's function for the tight-binding Hamiltonian using the direct summation method, which worked well for all distances but is computationally slow, or the Horiguchi recursive technique, which is a fast method but has stability problem for large $R \gtrsim 7a$ or so. For distances, where both methods worked, the results agreed with each other with no noticeable difference. These methods are complementary to the finite-lattice calculations;[7] however, the direct summation method allows the calculation of J for much larger distances with modest computational efforts. By carefully considering the phase factors of the wavefunctions around the Dirac cones, we have also obtained the analytical long-distance limits of J, Eqs. (23) and (30), which, although similar in form to previous results,[3,7] have important corrections in terms of additional phase factors in the oscillating term. All such phase factors were faithfully reproduced in our numerical calculations of J using the full tight-binding band structure. We found that the long-distance limit is reached for quite small distances, of the order of a few lattice constants.

In addition to the NN model, we have also studied the effect of the further-neighbor electron hopping, but these produced negligible differences as might be expected, since the strengths of the higher-neighbor hoppings are quite small in graphene.[9] For the hexagonal plaquette impurities, J is always antiferromagnetic, while for the bond impurities, the sign oscillates. Given that the magnitude of J falls off quite

rapidly with distance, NN J would dominate, so that spin chains based on hexagonal plaquette sites are predicted to be antiferromagnetic, while those based on the bond sites would be ferromagnetic.

In trying to design an experimental system to observe the RKKY interaction, one must carefully select a proper system. At first sight, it might appear that a magnetic adatom such as Co or Fe deposited on top of the graphene sheet would interact via the RKKY interaction. However, in addition to introducing the needed localized magnetic moments from the d electrons, the outermost s electrons of the adatom are transferred to the host, where either they are added to the conduction band or they may form weakly localized states around the adatom site. These extra electrons will modify the RKKY interaction. The challenge is therefore to come up with a system, perhaps a simple molecule, that has a magnetic moment interacting with the graphene lattice, but one that does not alter the electronic structure by contributing extra electrons to the graphene sheet. Because of this reason, there has been no proper study of the RKKY interaction using density-functional methods, even though interaction between magnetic impurities in graphene have been studied in several cases.[19–21] Also, because the density-functional methods involve supercell calculations, it is computationally difficult to study RKKY interaction for anything but small distances. As to the question whether one should have the Kondo moment formation or the RKKY interaction in graphene, one expects the RKKY interaction to dominate, since scaling arguments[22] as well as renormalization group calculations[23] indicate that an energy-linear density of states at the Fermi energy in graphene suppresses the Kondo effect below the critical coupling $J_c \approx 3.5$ eV, which is quite strong.

ACKNOWLEDGMENTS

This work was supported by the US Department of Energy through Grant No. DE-FG02-00ER45818. MS thanks A. T. Rezakhani for useful discussions.

[1] M. A. Ruderman and C. Kittel, Phys. Rev. **96**, 99 (1954); T. Kasuya, Prog. Theor. Phys. **16**, 45 (1956) ; K. Yosida, Phys. Rev. **106**, 893 (1957).
[2] B. Fischer and M. W. Klein, Phys. Rev. B **11**, 2025 (1975); M. T. Béal-Monod, *ibid.* **36**, 8835 (1987).
[3] S. Saremi, Phys. Rev. B **76**, 184430 (2007).
[4] L. Brey, H. A. Fertig, and S. Das Sarma, Phys. Rev. Lett. **99**, 116802 (2007).
[5] M. A. H. Vozmediano, M. P. López-Sancho, T. Stauber, and F. Guinea, Phys. Rev. B **72**, 155121 (2005).
[6] V. K. Dugaev, V. I. Litvinov, and J. Barnas, Phys. Rev. B **74**, 224438 (2006).
[7] A. M. Black-Schaffer, Phys. Rev. B **81**, 205416 (2010).
[8] J. E. Bunder and H.-H. Lin, Phys. Rev. B **80**, 153414 (2009).
[9] B. R. K. Nanda and S. Satpathy, Phys. Rev. B **80**, 165430 (2009).
[10] C. Bena and G. Montambaux, New J. Phys. **11**, 095003 (2009).
[11] T. Horiguchi, J. Math. Phys. **13**, 1411 (1972).
[12] M. Berciu, J. Phys. A: Math. Theor. **42**, 395207 (2009).
[13] T. Morita and T. Horiguchi, Numer. Math. **20**, 425 (1973).
[14] S. Zhang and J. Jin, *Computation of Special Functions* (Wiley, New York, 1996).
[15] I. S. Gradshteyn and I. M. Ryzhik, *Tables of Integrals, Series, and Products* (Academic Press, New York, 1980), Secs. 8.451.6 and 8.511.4.
[16] Z. F. Wang, R. Xiang, Q. W. Shi, J. Yang, X. Wang, J. G. Hou, and J. Chen, Phys. Rev. B **74**, 125417 (2006).
[17] C. Bena, Phys. Rev. B **79**, 125427 (2009).
[18] M. Abramowitz and I. A. Stegun (Eds.) *Handbook of Mathematical Functions with Formulas, Graphs, and Mathematical Tables* (National Bureau of Standards, Washington, DC, 1972), p. 374.
[19] E. J. G. Santos, D. Sánchez-Portal, and A. Ayuela, Phys. Rev. B **81**, 125433 (2010).
[20] Y. Mao, J. Yuan, and J. Zhong, J. Phys.: Condens. Matter **20**, 115209 (2008).
[21] P. O. Lehtinen, A. S. Foster, A. Ayuela, A. Krasheninnikov, K. Nordlund, and R. M. Nieminen, Phys. Rev. Lett. **91**, 017202 (2003).
[22] D. Withoff and E. Fradkin, Phys. Rev. Lett. **64**, 1835 (1990).
[23] B. Uchoa, T. G. Rappoport, and A. H. Castro Neto, Phys. Rev. Lett. **106**, 016801 (2011).